Int. J. Electrochem. Sci., 15 **(2020)** 9948 – 9970, doi: 10.20964/2020.10.40

International Journal of
ELECTROCHEMICAL
SCIENCE
www.electrochemsci.org

Corrosion Evolution of a Concrete/Casing Steel in Simulated Formation Water under Different CO_2 Partial Pressures

Shuliang Wang[1,3], *Mengjun Yao*[1], *Xujia He*[1], *Bensong Wu*[1], *Li Liu*[1], *Shidong Wang*[2,3,*],
Mingyu Wu[3,4,*], *Xingguo Zhang*[5], *Dinghan Xiang*[6]

[1] School of New Energy and Materials, Southwest Petroleum University, Xindu Avenue 8#, Sichuan 610500, China
[2] Northwestern Polytechnical University, Xi'an, 710072, China
[3] Department of Chemical and Materials Engineering, University of Alberta, Edmonton, Alberta T6G 2G6, Canada
[4] School of Materials Science and Engineering, Shanghai University, 149 Yanchang Road, Shanghai 200072, China
[5] School of Petroleum Engineering, Southwest Petroleum University, Chengdu 610500, P.R. China
[6] Guangxi Key Laboratory of Information Materials, Guilin University of Electronic Technology, Guilin 541004, PR China
[*]E-mail: shidong@ualberta.ca (S.D. Wang), mingyu8@ualberta.ca (M.Y. Wu)

Received: 11 June 2020 / *Accepted:* 1 August 2020 / *Published:* 31 August 2020

The corrosion behavior, mechanical properties, and microstructural evolution of a concrete/P110 casing steel system were studied in a simulated, CO_2-saturated formation water under different CO_2 partial pressures. It has been found that the corrosion and mechanical properties of the cement and the cement/casing interface were affected by both cement hydration and CO_2 corrosion, making the performance of the cement matrix and the interfacial transition zone improve initially and then deteriorate with time. The corrosion resistance of the casing steel reduced with increasing the immersion time and CO_2 pressure. The degradation of cement and cement/casing interface was aggravated under the high CO_2 pressure, which assisted the formation of a defected corrosion product layer (predominantly $Fe_xCa_{1-x}CO_3$) and led to severer corrosion on the casing steel surface.

Keywords: Steel; CO_2; Corrosion; EIS; Interfacial transition zone

1. INTRODUCTION

In the oil and gas industry, the life of cement/casing system is of great significance for the safe exploitation of oil and gas resources. The well cement normally consists of many pores where a highly alkaline pore liquid presents, facilitating the passivation of casing steel wrapped by the cement ring [1-

4]. Therefore, the casing steel in the cement could retain its corrosion resistance before the breakdown of the passive film [5, 6].

In recent years, many countries start to focus on deep wells and ultra-deep wells due to the lack of the oil and gas resources. The resources in the deep and ultra-deep wells are covered with a salt-gypsum layer, where the brine cement slurry is extensively used to prevent wellbore collapse due to a large amount of salt dissolved into the slurry [7]. The concentration of salt in the brine cement slurry has a significant effect on the properties of the cement and casing steel [8-10]. The high salt content (with a NaCl content of ~ 36% by weight of water) in saturated brine cement slurry retards the hydration, decreases the strength development, and increases the permeability of the cement. The passivation of the casing steel is reduced due to the high content of Cl^- in the surrounding cement [9]. As is reported, semi-saturated brine cement slurry has the potential to yield the greatest desired properties of the cement, which is beneficial to the well integrity [11, 12]. Also, a lower tendency of the passive film breakdown on the casing steel is expected using the semi-saturated brine cement slurry.

The corrosion of the cement/casing is detrimental to the safe exploitation of oil and gas resources in the deep wells and ultra-deep wells [13, 14]. Although many efforts have been made on the corrosion research of oil well cement and/or casing steel, the corrosion mechanism of cement/casing system, especially the interface stability between cement and casing steel, are scarcely reported [15-22].

Carbon dioxide (CO_2), which is distributed in various oil and natural gases, has been acknowledged to be a major corrosion source for the failure of cement and casing steels. CO_2 is corrosive to cement under the appropriate humidity (relative humidity higher than 50%) and pressure [12], which decreases the alkalinity of the electrolyte in the cement pores and the strength of cement ring, and increases the porosity of the cement ring. In the presence of CO_2, a layer of non-protective $FeCO_3$ corrosion products would form on the steel surface, which will induce the formation of localized corrosion depending on the coverage rate and integrity of the $FeCO_3$ layer [23-27]. In addition, the corrosion rate of steel was found relatively low when the CO_2 concentration or partial pressure is high [28]. It was because the scale that formed on the steel was denser and had superior surface coverage, which results in a decrease in the corrosion rate. For a saturated brine cement/casing system in CO_2-saturated formation water, however, the casing steel surface and the interface between cement and casing steel were found deteriorated after 2-month of corrosion [9]. The above literature review indicates that CO_2 could either accelerate or decelerate the corrosion rate of the steel depending on its partial pressure. The corrosion mechanism of the steel in a cement/steel system is not well established [22, 29]. To the authors' knowledge, no studies have been reported about the effect of CO_2 and its partial pressure on the corrosion of a semi-saturated brine cement concrete/ P110 casing steel system in the simulated formation water.

In this work, a semi-saturated brine cement concrete/P110 casing steel system was used to study its corrosion evolution in a synthetic formation water saturated with CO_2. Specially, the effect of CO_2 pressure on the corrosion of cement/casing and the instability phenomenon at the interface of cement/casing will be investigated.

2. EXPERIMENTAL

2.1 Sample preparation

Aksu G-grade cement and P110 casing steel were used to prepare the cement concrete/casing steel system. The composition of the semi-saturated brine cement slurry is as follows (in gram): cement: 520, water: 222, salt: 15, ganister: 130, microsilicon: 26, dispersant: 30.72, and anti-gas channeling agent: 10.14. For the cement/casing system, a casing steel with a diameter of 10 mm and working end length of 40 mm was coated with the cement concrete, as shown in Figure 1 (a). One end of the casing steel has an external thread which was attached with a copper wire for electrochemical measurement. With the addition of a defoaming agent, the cement slurry was stirred vigorously, and then poured and solidified in a mold with the P110 steel located in the center under the controlled temperature of 80°C. The cement samples with a diameter of 50 mm and length of 110 mm were demolded after curing for 24 hours. Note that the term cement/casing refers to cement concrete/casing steel or concrete/casing steel in this work.

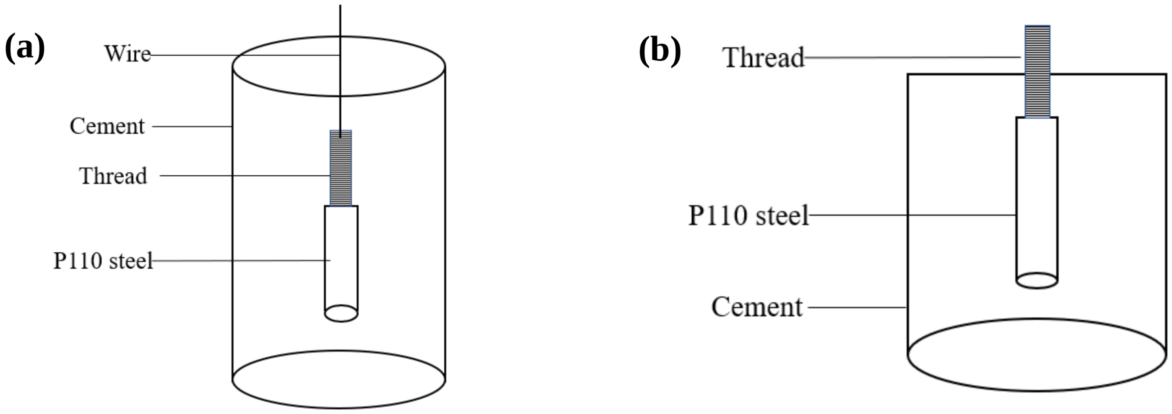

Figure 1. Sketch map of the cement/casing sample for (a) immersion and electrochemical measurement, and (b) mechanical tests.

2.2 Immersion test

The immersion test was performed in a static autoclave. The composition of the simulated formation water was as follows: Na^+: 1941.55, K^+: 72.12, Ca^{2+}: 140.28, Mg^{2+}: 82.05, Cl^-: 2430.88, HCO_3^-: 280.04 and SO_4^{2-}: 120.02 (in mg/l). The simulated formation water was poured into the autoclave, and then N_2 gas was bubbled for 4 h to remove oxygen before CO_2 was introduced in the autoclave. The solution was purged with CO_2 for 4 h to make it saturated with CO_2. Two different CO_2 pressures were employed in the tests to investigate the CO_2 effect: 1) under normal pressure, i.e. CO_2 pressure was 0.1 MPa, and 2) under high pressure (8 MPa, CO_2 partial pressure was 2 MPa, and N_2 balanced). The temperature was controlled at 80°C. The prepared cement/casing samples were immersed in the aforementioned autoclaves for 10-60 days.

2.3 Electrochemical test

Electrochemical tests were carried out with the PGSTAT302N Autolab electrochemical workstation. A three-electrode system was employed with the cement/casing sample as a working electrode, the platinum plate as an auxiliary electrode, and the saturated calomel electrode (SCE) as a reference electrode. After each immersion test for 10-60 days, the sample was removed and then quickly assembled in the three-electrode cell for electrochemical testing. The testing solution was the simulated formation water saturated with CO_2 at a controlled temperature of 80°C. The surface area of the casing steel was 12.56 cm^2. The AC impedance test (EIS) was performed at the open circuit potential (OCP), and the EIS scanning frequency ranged from 100 kHz to 10 mHz with an AC amplitude of 10 mV (peak-to-zero). At least three tests were carried out for each condition to ensure the reproducibility.

2.4 Mechanical test

The threaded part of the cement/casing sample was exposed (Figure 1 (b)) and connected by a special fixture, and the other end of the sample was connected by a sleeve. A pull-out method was utilized to measure the shearing force of the interface between the cement and the casing steel by a material mechanical testing machine. The maximum tensile stress was recorded and then converted into the interfacial shear strength to evaluate the cementation strength of the interface. Vickers hardness of the cement ring and the area near the interface between cement and casing steel (i.e. the interfacial transition zone) was measured after the cement sample was transversely sectioned and polished. The load for the measurement was 300 gf, and the duration was 10 s. Compressive strength test of the corroded samples was carried out using a pressure tester. The compressive strength was calculated with the maximum compressive stress recorded at the cracking of the cement and the original cross-sectional area of the test sample. Afterwards, the fracture surface of the failed cement samples was observed using SEM. For each test, at least two samples were used to ensure the reproducibility.

2.5 Post-test analysis

After the tests, microstructural evolution of the cement stone and casing steel was observed by ZEISS EVO MA15 scanning electron microscope (SEM) equipped with an energy spectrometer (EDS) at an acceleration voltage of 20 kV. The composition of the corrosion products on the steel surface was measured by Raman spectroscopy with a measurement range of 200 cm^{-1}-1200 cm^{-1} and a step size of 2 cm^{-1}. Afterwards, the corrosion products were measured by x-ray photoelectron spectroscopy (XPS) with the efficiency and energy voltage of 12 kV, and the vacuum degree during sputtering of 2.0×10^{-7} mba.

3. RESULTS AND DISCUSSION

3.1 Electrochemical impedance spectroscopy (EIS) analysis

Figure 2 shows the EIS curves of samples with different immersion time under normal pressure. During the entire course of corrosion, the Nyquist plots consist of two capacitive loops respectively in the high and medium-frequency ranges and a diffusion tail in the low-frequency range (Figure 2 (a)). It has been well accepted that the high-frequency capacitive loop represents the microstructural variation of the cement [30]. The medium or low-frequency capacitive loop reflects the dissolution processes at the steel/cement interface. The low-frequency diffusion tail is related to the diffusion process of corrosive species, indicating the corrosion process is controlled by the diffusion of corrosive species through the cement layer or passivation film of the casing steel [31]. It can be found that the high-frequency capacitive loops enlarge first and then shrink with prolonging the immersion time, whereas the low-frequency capacitive loops keep decreasing with time. These results reveal that the corrosion rate of the casing steel is increasing with time although its outer cement can block the solution to some extent.

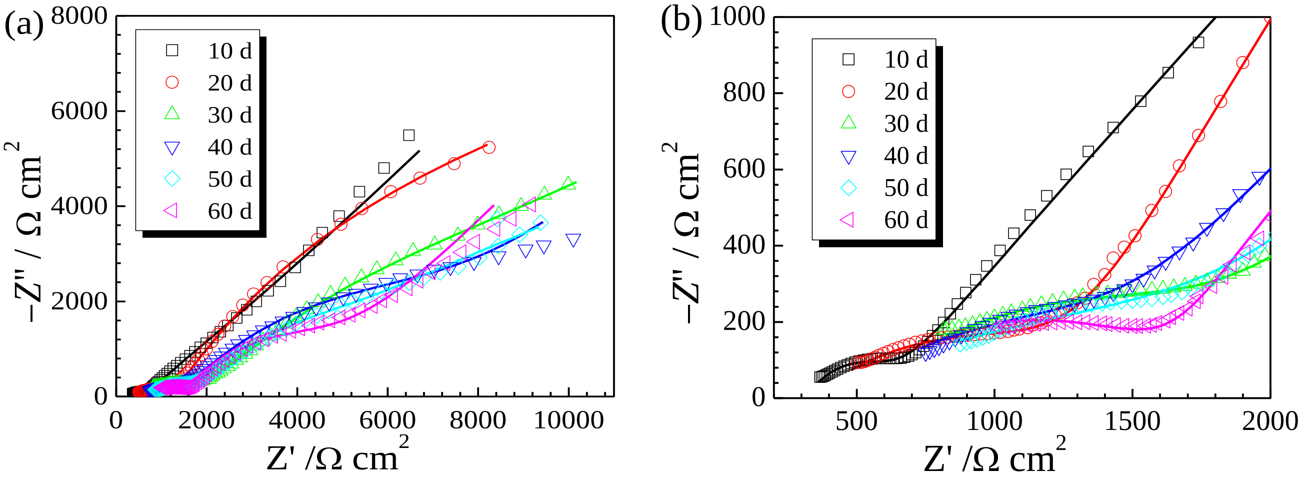

Figure 2. Electrochemical impedance spectra of samples in CO_2-saturated formation water at 80°C after immersion with various immersion time under normal pressure: (a) Nyquist plots and (b) an enlargement of image (a)

In order to fit the EIS data, a simple electrochemical equivalent circuit model was utilized, as shown in Figure 3 [32]. R_s is the solution resistance; R_c and Q_c are respectively the resistance and constant phase element (CPE) of the cement layer; R_{ct} and Q_{dl} are respectively the charge transfer resistance and CPE of the electric double layer on the surface of the casing steel. W is the Warburg impedance describing the transport of corrosive species. CPE is used in this work as a substitute for a capacitor to compensate for the nonideal capacitive response. The CPE impedance can be expressed as: $Z_{CPE}=[Q(j\omega)n]^{-1}$, where Q is the constant of CPE, ω is the angular frequency, and n is the dispersion coefficient of CPE ($0<n\leq1$) [33]. According to the proposed equivalent circuit model, all the EIS curves were fitted and the fitting parameters are listed in Table 1. The resistance of the cement layer (R_c) is 304 Ω cm² at the immersion time of 10 days. It increases with time and reaches a maximum value of 1785

Ω cm^2 at 40 days, and then declines slowly to 1254 Ω cm^2 at 60 days. The corrosion of cement is influenced by both the hydration and carbonation processes of cement [22, 32, 34]. The former process improves while the latter decreases the stability and corrosion resistance of the cement layer. When the immersion time is less than 40 days, the hydration process is dominant, which makes the cement structure become denser with time. When the time exceeds 40 days, the hydration process may slow down and the carbonation of cement becomes the dominant process. The carbonation destroys the original structure of the cement, leading to an increase of porosity and permeability of the cement. For instance, the CO_2-related species could react with the hydration product $Ca(OH)_2$ to form $CaCO_3$ and even $Ca(HCO_3)_2$, depending on the concentration of CO_2 [32]. The charge transfer resistance (R_{ct}) shows a maximum value of 15.9 kΩ cm^2 at the immersion time of 10 days, and then it decreases gradually with time. After 60 days of immersion, the value decreases to 3.5 kΩ cm^2. The decrease in the R_{ct} can be rationalized as follows: 1) a passivation film was formed on the casing steel surface in the highly alkaline environment (pore solution of the cement) in the early stage, which reduces the corrosion rate [2, 3]; 2) with prolonging the immersion time, the penetration of corrosive species such as CO_3^{2-}, HCO_3^- and Cl^- from solution to the interface of cement/casing could occur, which breaks the passivation film [35]; and 3) the carbonation process decreases the pH of the electrolyte trapped around the steel, which further increases the corrosion rate of the casing steel [36].

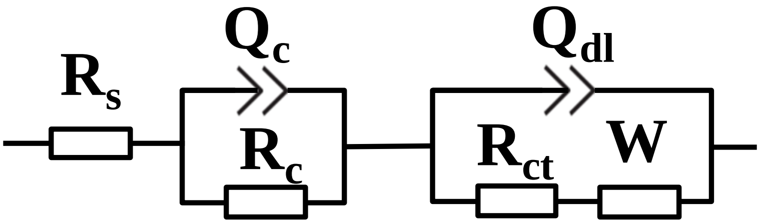

Figure 3. Equivalent circuit model of the samples in different corrosion stages

Table 1. Fitting results of the EIS for samples in CO_2-saturated formation water at 80°C after immersion with various immersion time under normal pressure.

Time (d)	R_s (Ω cm^2)	Q_c ($S \cdot sec^n/cm^2$)	n_c	R_c (Ω cm^2)	Q_{dl} ($S \cdot sec^n/cm^2$)	n_{dl}	R_{ct} (Ω cm^2)	W ($S \cdot sec^{0.5}/cm^2$)	$\chi^2 \times 10^4$
10	318	1.4×10^{-5}	0.57	304	3.8×10^{-4}	0.47	15930	1.3×10^{-4}	3.71
20	326	7.0×10^{-5}	0.33	1126	4.6×10^{-4}	0.66	15530	8.1×10^{-4}	1.25
30	483	2.6×10^{-5}	0.36	1550	2.4×10^{-4}	0.50	15180	8.2×10^{-4}	1.00
40	359	8.6×10^{-5}	0.26	1785	1.8×10^{-4}	0.58	8039	1.1×10^{-3}	3.62
50	407	5.6×10^{-5}	0.31	1475	1.5×10^{-4}	0.60	7100	9.0×10^{-4}	1.49
60	498	1.1×10^{-5}	0.39	1254	8.8×10^{-5}	0.68	3473	7.1×10^{-4}	3.31

Figure 4 shows the EIS curves of samples with different immersion time under the high pressure. Two capacitive loops respectively in the high and medium-frequency ranges and a diffusion tail in the low-frequency range are visible in the Nyquist plots, which is similar to the feature of the plots under the normal pressure. The variation trends of the high-frequency and medium-frequency capacitive loops with immersion time are also consistent with that under the normal pressure.

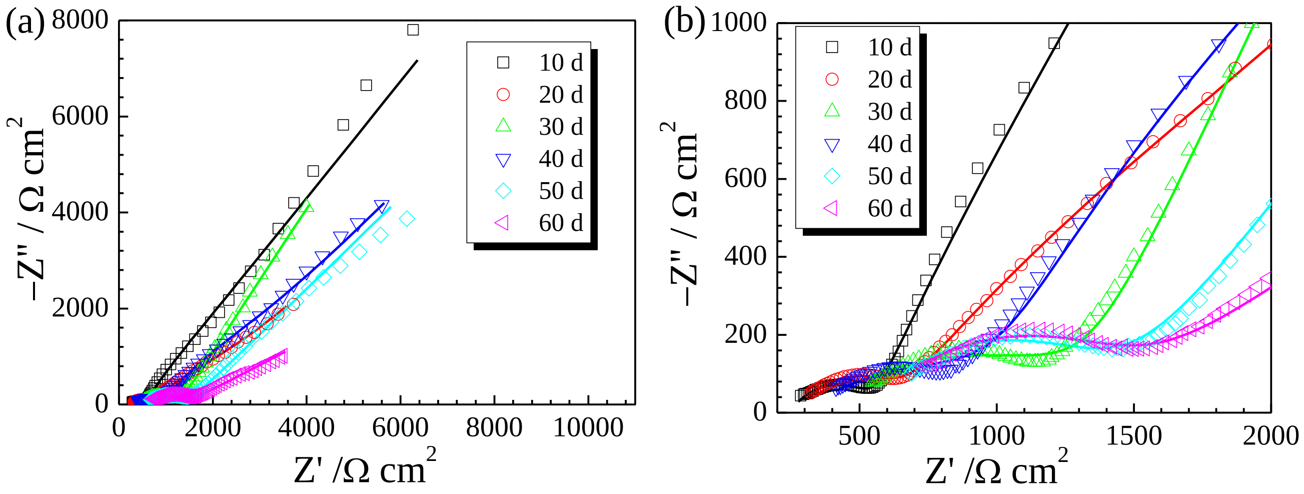

Figure 4. Electrochemical impedance spectra of samples in CO_2-saturated formation water at 80°C after immersion with various immersion time under high pressure: (a) Nyquist plots and (b) an enlargement of image (a)

Table 2. Fitting results of the EIS for samples in CO_2-saturated formation water at 80°C after immersion with various immersion time under high pressure.

Time (d)	R_s (Ω cm^2)	Q_c ($S\cdot sec^n/cm^2$)	n_c	R_c (Ω cm^2)	Q_{dl} ($S\cdot sec^n/cm^2$)	n_{dl}	R_{ct} (Ω cm^2)	W ($S\cdot sec^{0.5}/cm^2$)	$\chi^2\times10^4$
10	244	2.4×10^{-5}	0.51	322	3.6×10^{-4}	0.69	4271	2.0×10^{-4}	3.09
20	259	1.6×10^{-5}	0.53	326	6.5×10^{-4}	0.41	4200	2.9×10^{-4}	0.99
30	343	9.6×10^{-5}	0.31	1227	9.9×10^{-4}	0.87	2737	6.2×10^{-4}	2.37
40	276	1.7×10^{-4}	0.27	983	4.6×10^{-4}	0.67	2628	4.1×10^{-4}	3.52
50	502	1.8×10^{-5}	0.44	954	5.2×10^{-4}	0.48	871	1.3×10^{-4}	2.82
60	527	2.0×10^{-5}	0.44	932	9.5×10^{-4}	0.30	839	4.9×10^{-5}	1.86

The same electrochemical equivalent circuit model (Figure 3) was used to fit the EIS data and the fitting parameters are listed in Table 2. The R_c value is 322 Ω cm^2 (10 days) and increases to the maximum value of 1227 Ω cm^2 at 30 days. Then, it decreases gradually to 932 Ω cm^2 at 60 days. Compared with that under the normal pressure, it takes less time to reach the maximum value under the high pressure. In addition, the R_c values of the latter are always smaller than that of the former when the immersion time has exceeded 20 days. It may be because high pressure could accelerate the hydration and carbonation processes of cement [29, 34]. The carbonation process is more pronounced under the high pressure (with a high partial pressure of CO_2), thereby reducing the corrosion resistance of the cement. The R_{ct} shows a maximum value of 4.3 kΩ cm^2 (10 days), and then decreases gradually with time. After 60 days of immersion, it decreases to 0.8 kΩ cm^2 which is only 0.24 times as compared to that under the normal pressure. During the entire course of corrosion, the R_{ct} value under the high pressure is less than one third as compared to that under the normal pressure. These results imply that the high pressure facilitates not only the carbonation process of cement but also the diffusion of CO_2-related species and Cl^- through the cement, which would cause a faster accumulation of CO_2-related species and Cl^- at the interface of cement/casing and degradation of the casing steel.

3.2 Mechanical properties evaluation

3.2.1 Shear strength

Figure 5 shows the variation of interfacial shear strength for the cement/casing system with time. Under normal pressure condition, the interfacial shear strength between the cement and casing steel increases and reaches a maximum value of 2.4 MPa at 40 days of immersion. It clearly reveals that the cementing ability between the cement and casing gradually increased for the first 40 days. It implies that the interface of cement/casing may be only marginally damaged due to the carbonation in the first 40 days. On the contrary, the bonding strength between cement and casing should increase owing to the hydration of cement, which could be verified by the morphology variation of the interface of cement/casing later. After 40 days of immersion, the value of interfacial shear strength decreases with time. It means the carbonation of cement and corrosion attack of casing steel have become dominant after 40 days, which severely corrodes the interface and decreases the cementing ability between the cement and casing steel. In comparison to the EIS results, the variation trend of interfacial shear strength is consistent with that of the R_c values. It suggests that the degradation of interfacial shear strength begins when the cement cannot provide sufficient protection, whereby corrosion initiates at the cement/casing interface.

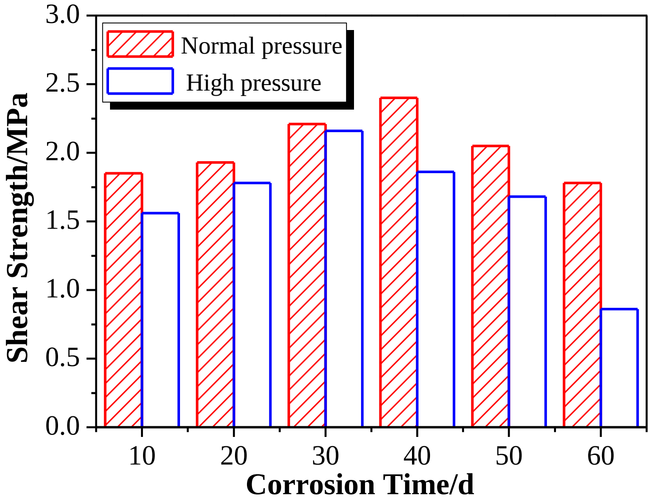

Figure 5. Variation of shear strength of cement/casing system after immersion in CO_2-saturated formation water with different immersion time under normal and high pressure conditions

Under the high pressure, a similar trend of the shear strength is observed as that under the normal pressure. The differences are that it takes less time (30 days) for the interfacial shear strength to reach the transition point (transition from strengthening to weakening), and the strength values are invariably smaller under the high pressure. After 60 days under the high pressure, the interfacial shear strength decreases to 0.86 MPa, which implies that the cementation strength at the interface of cement/casing is basically lost. It manifests that high pressure accelerates the penetration rate of CO_2-related species and Cl^- in the cement, which reduces the time for them to reach and accumulate at the interface, leading to much severer corrosion at the interface [37]. This is consistent with the electrochemical result that the decrease of R_{ct} value with time for the sample under the high pressure is more pronounced (Table 1 and Table 2).

3.2.2 Cement microhardness

It has been reported that a loose and weak transition zone exists at the interface between cement and casing steel, which contains a large number of easily erodible $Ca(OH)_2$ crystals, highly alkaline C-S-H gel and unhydrated cement particles [38]. In order to reveal the difference in mechanical property between the interfacial transition zone and matrix of cement, the variations of microhardness in the two different regions are shown in Figure 6. Under normal pressure condition, the microhardness values of both the cement matrix and the interfacial transition zone tend to increase slowly up to 40 days, and then decrease with time. Based on the analysis of hydration and carbonation characteristics of the cement in the corrosion process in the CO_2-containing formation water [39], it is believed that both the hydration and carbonation processes have an impact on the performance of the cement. For the first 40 days of immersion, the microhardness increases when the hydration of cement is dominant, which increases the density and stability of the cement. After 40 days of immersion, the density of cement declines due to the carbonation-induced pores or defects in the cement, leading to a decrease in the microhardness [32]. These analyses could be verified later by the microstructural evolution of the cement stone with immersion time. It is also found that the microhardness of the cement matrix is always higher than that of the interfacial transition zone, as shown in Figure 6 (a). The lower hardness of the interfacial transition zone is mainly ascribed to: 1) the hydration degree of the interfacial transition zone is lower than that of the matrix in the early stage of immersion, and 2) CO_2-related species penetrate through the cement and largely accumulates in the interfacial transition zone in the later stage of immersion, which causes severe corrosion and degradation of cement in the interfacial transition zone.

Under the high-pressure condition, the value of microhardness also increases initially and then decreases with time, as shown in Figure 6 (b). The microhardness of the interfacial transition zone is invariably lower than that of the matrix of cement. However, the microhardness of both cement matrix and the interfacial transition zone reaches the maximum value at the time of 30 days, which is shorter than the time used under the normal pressure. In addition, the microhardness values of both cement matrix and the interfacial transition zone are higher under the high pressure than that under normal pressure during the entire course of immersion. It clearly indicates that high pressure increases the rate and extent of hydration of the cement [34], leading to higher microhardness values. However, the high pressure (with a high CO_2 partial pressure) also increases the carbonation rate of cement and the diffusion rate of CO_2-related species through the cement, resulting in an earlier degradation of the cement as well as the interfacial transition zone.

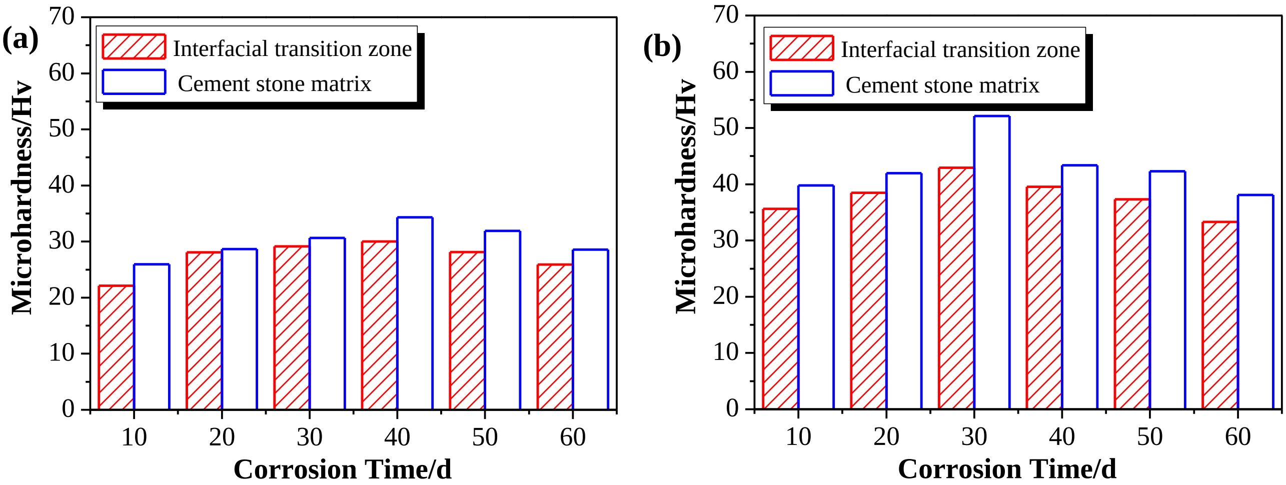

Figure 6. Variation of microhardness of cement stone after immersion in CO_2-saturated formation water with different immersion time: (a) under normal pressure condition, and (b) under high pressure condition

3.2.3 Compressive strength

Figure 7 shows the variation of compressive strength for the cement stone with time under normal and high pressure. The compressive strength of cement increases slowly till 40 days of immersion and then declines with time under the normal pressure, which is consistent with the trend of its microhardness. The explanation of this trend is similar to that of the microhardness. In the initial stage of immersion, the rapid hydration and hardening of cement increase the compressive strength with time, whereas the carbonation caused a reduction in the strength is negligible because the carbonation process is limited to the outer layer of cement stone (could be validated with the microstructural evolution of cement stone in the following Figure 8). After 40 days of immersion, carbonation has become the predominant process whereas the cement hydration rate has reduced, the combined effect of which decreases the compressive strength. Similar results were reported by Zhang *et al.* [9]. They found that the maximum compressive strength of a saturated brine cement concrete was at ~ 40 days of immersion under the normal pressure, and then it degraded with increasing immersion time [9]. Under the high pressure, the compressive strength of cement reaches its maximum value after 30 days of immersion which is shorter than that under the normal pressure (40 days). After 30 days of immersion, the compressive strength decreases with time. It is interesting that the compressive strength under the high pressure is higher than that under the normal pressure before 20 days of immersion, whereas the compressive strength of the former is lower than that of the latter after 30 days of immersion. It is generally accepted that the compressive strength of concrete increases sharply before ~ 30 days of curing because of the hydration, and then its value increases slowly with time [34, 40, 41]. The carbonation process normally could result in a strong decrease of resistivity and higher porosities of the concrete, which accelerates the conversion of carbonates into bicarbonates, and therefore leads to the degradation of the concrete strength [32, 42, 43]. These facts manifest that the high pressure is beneficial for the fast hydration and hardening of the cement which increases the compressive strength [14, 34]. However, it also accelerates the carbonation process and permeation of CO_2-related species in the cement, which deteriorates the compressive strength rapidly [32].

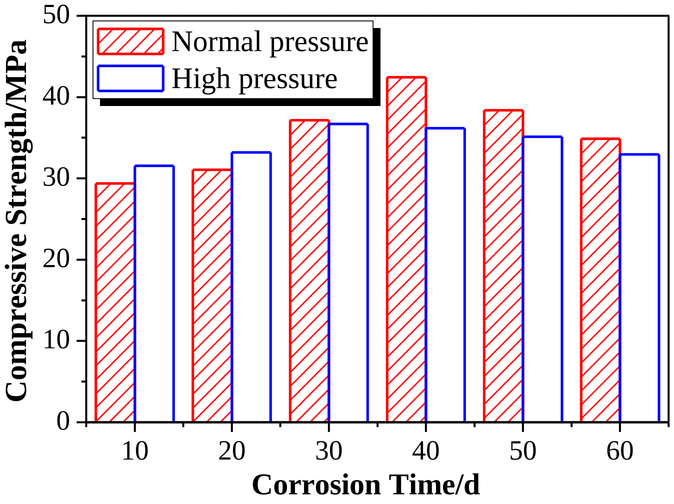

Figure 7. Variation of compressive strength of cement stone after immersion in CO_2-saturated formation water with different immersion time under normal and high pressure conditions

3.3 Microstructural evolution during the test

3.3.1 Fracture surface morphology of the cement stone

Figure 8 shows the fracture surface morphology of the cement stone after immersion for various times under the normal pressure condition. The fracture surface morphologies are similar both in the interfacial transition zone and the matrix of cement stone after 10 days of immersion, indicating the corrosion has not significantly affected the cement matrix and the interfacial transition zone (Figure 8 (a-b)). After 30 days of immersion, bonded $CaCO_3$ could only be occasionally found on the cement matrix, as shown in Figure 8 (d). In this stage, a small amount of $CaCO_3$ could be formed because of the low concentration of the CO_2-related species in the cement matrix. The chemical reaction mechanism is shown in Eq. (1) [44].

$$Ca(OH)_2 + HCO_3^- + H^+ \rightarrow CaCO_3 + 2H_2O \qquad (1)$$

Wigand *et al.* indicated that the formation of a small amount of $CaCO_3$ was beneficial if it had reduced the density of the pores in concrete [13]. However, a further carbonation and leaching effect would cause dissolution of the concrete and therefore increase the density of pores in the concrete [32, 45].

The penetration and accumulation of CO_2-related species will increase its concentration in the cement, thereby decreasing the pH value and the stability of the calcium silicate hydrate (CSH) and ettringite (Eq. (2)) [13]. After 40 days of immersion, micro pores are visible in the matrix of the cement stone because of the carbonation and leaching of the cement (Eqs. (3-4)), as shown in Figure 8 (f) [32]. The pores are enlarged and become more appreciable at the time of 60 days (Figure 8 (h)), which destroys the effectiveness of the cement. The relevant reactions can be expressed by Eqs. (2)-(4) [13].

$$CSH+H^{+} + HCO_3^{-} \rightarrow CaCO_3+SiO_2+ H_2O \qquad (2)$$

$$CO_2+ H_2O + CaCO_3 \rightarrow Ca(HCO_3)_2 \qquad (3)$$

$$Ca(HCO_3)_2+Ca(OH)_2 \rightarrow 2CaCO_3+2H_2O \qquad (4)$$

After 40 days of immersion, few strip-like crystals could be observed in the interfacial transition zone, as shown in Figure 8 (e). EDS result shows that it consists mainly C, O and Ca and a small amount of Si and Cl (Table 3). Based on atomic ratio calculation, the main composition of the crystal is determined to be $CaCO_3$, which is in good agreement with previous results [46]. It implies that the decrease of cementation strength resulting from the carbonation of the cement must have affected the interface of cement/casing after 40 days of immersion, which is consistent with the results of interfacial shear strength. In previous research, it was found that the interfacial transition zone started to degrade after about 30 days of immersion in the formation water containing CO_2. After 60 days of immersion, a large number of $CaCO_3$ precipitates were visible in the interfacial transition zone while the basic structure of the cement matrix had been severely damaged [9].

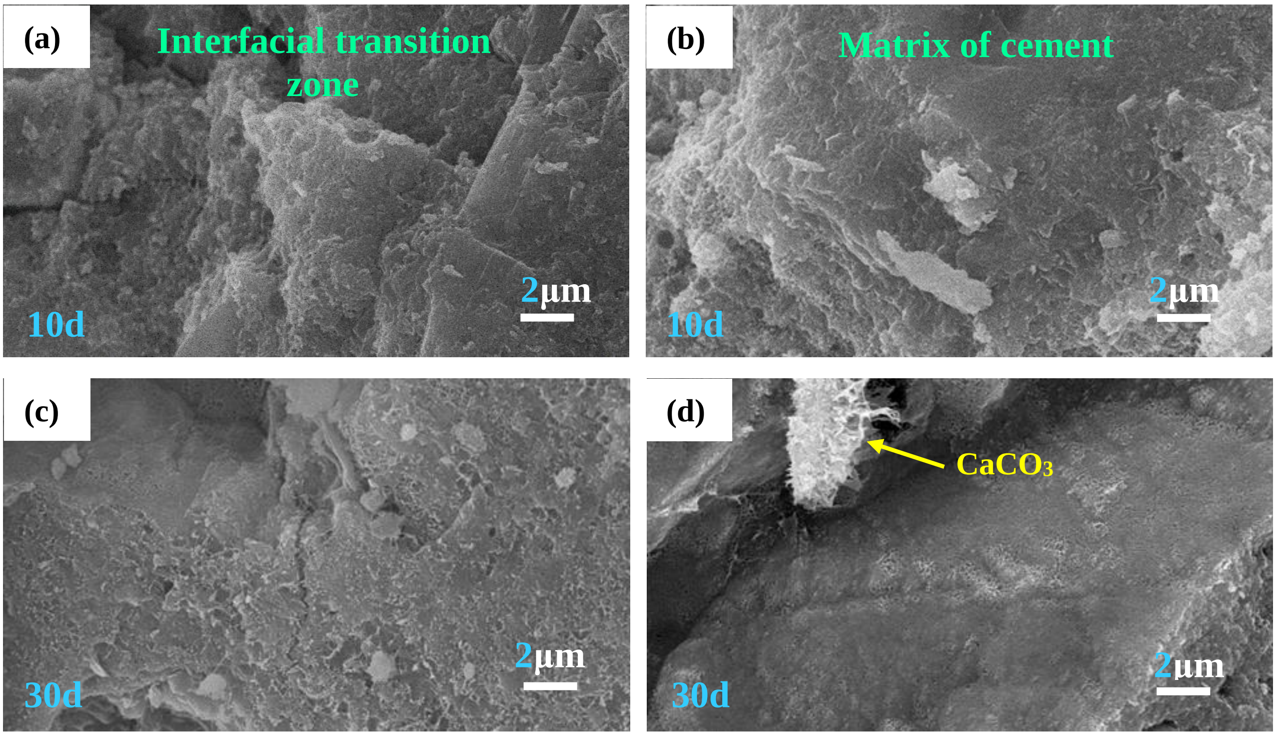

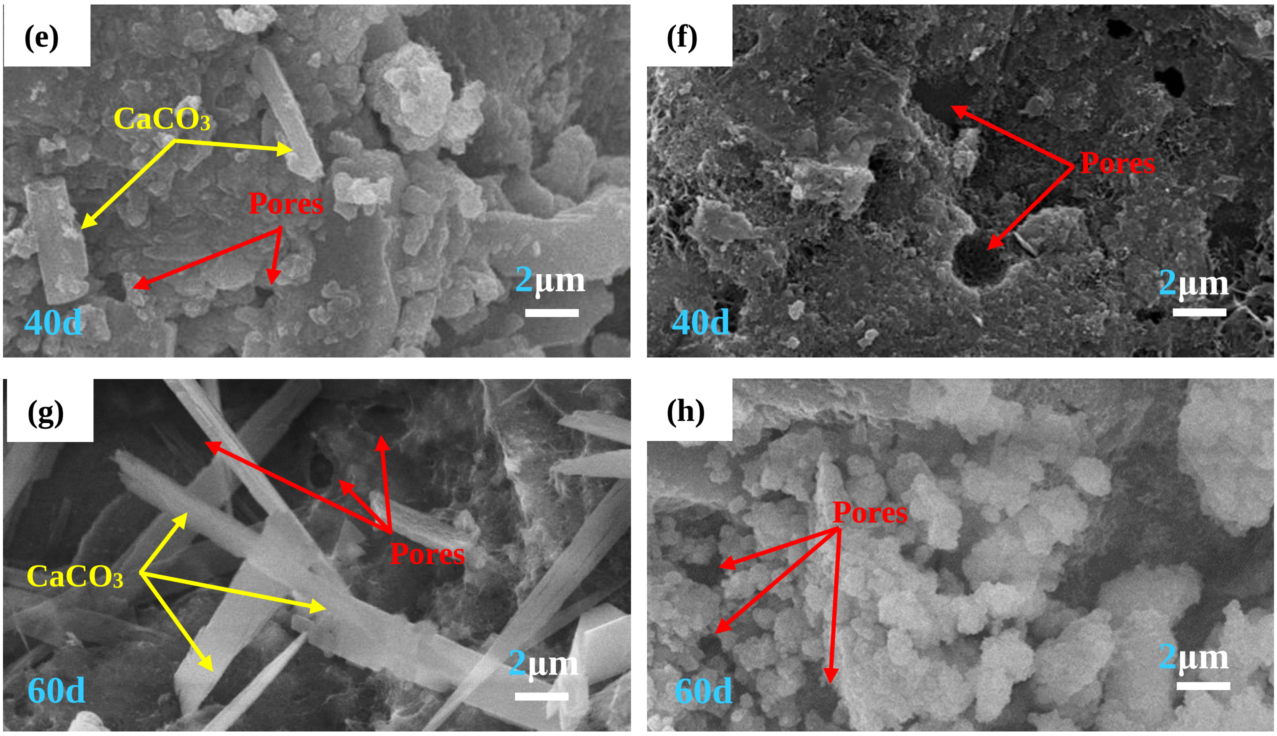

Figure 8. Fracture surface morphology of the cement stone at different locations after immersion in CO_2-saturated formation water at 80°C under normal pressure: (a) 10 d, interfacial transition zone; (b) 10 d, matrix; (c) 30 d, interfacial transition zone; (d) 30 d, matrix; (e) 40 d, interfacial transition zone; (f) 40 d, matrix; (g) 60 d, interfacial transition zone; and (h) 60 d, matrix.

Table 3. EDS result of the strip-like crystals in the interfacial transition zone

Element	C	O	Ca	Si	Cl
wt· %	10.6	45.8	35.6	6.1	1.9
at· %	18.1	58.3	18.1	4.4	1.1

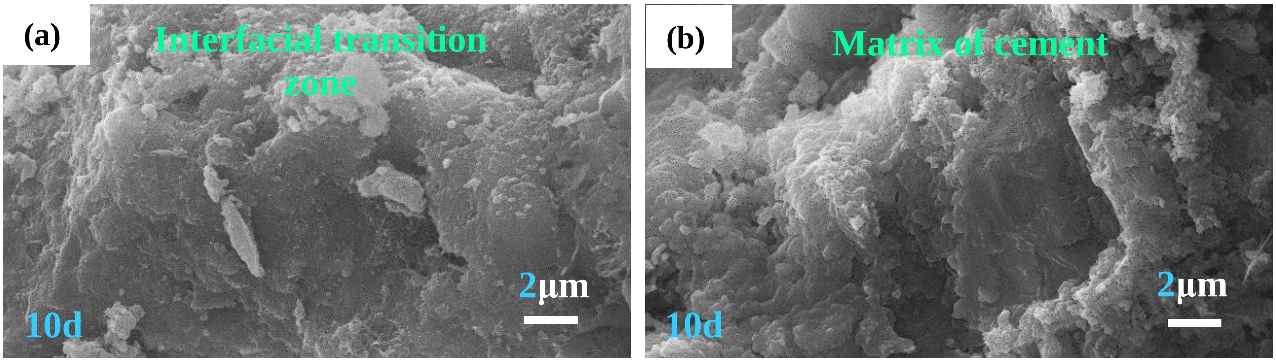

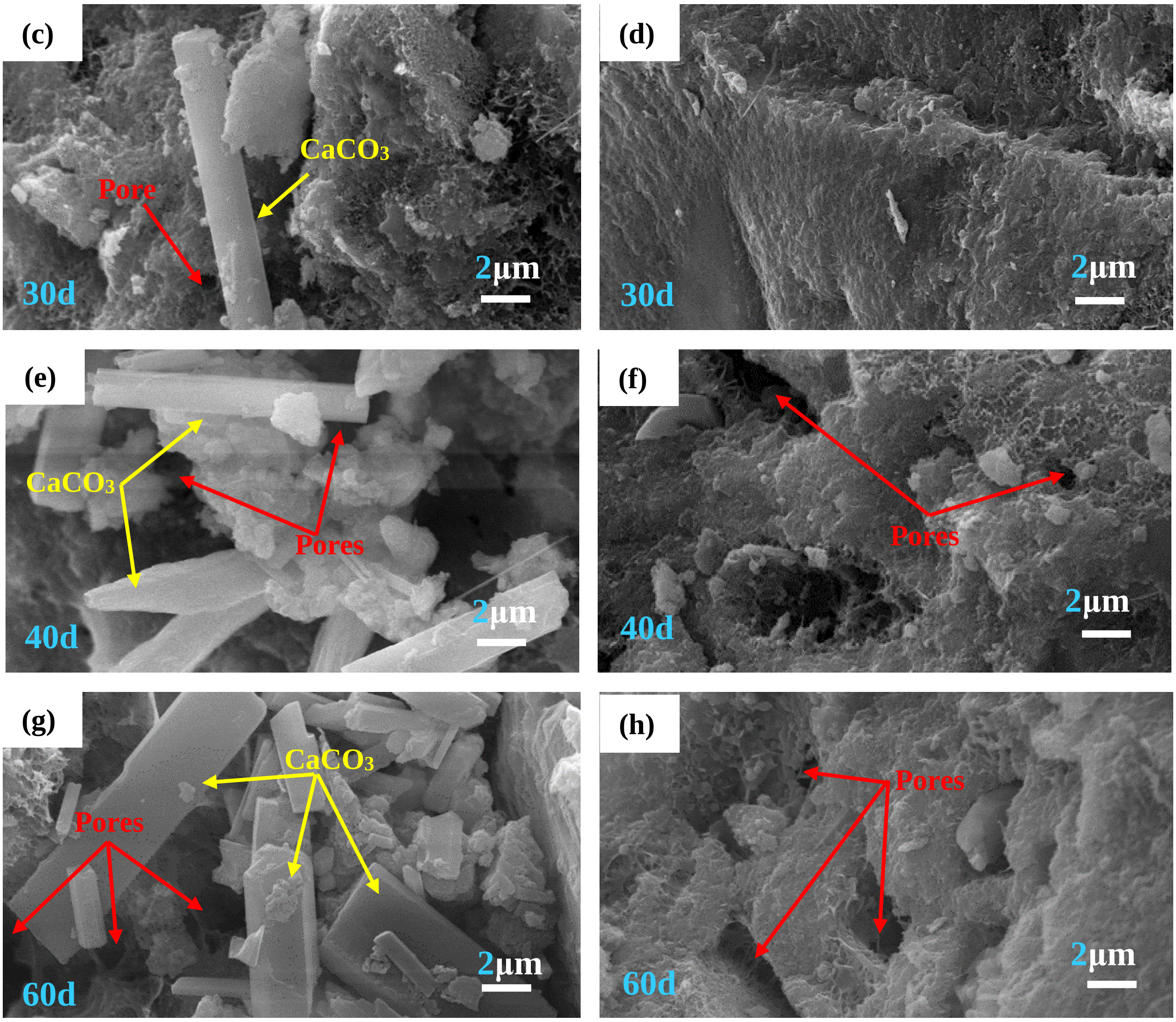

Figure 9. Fracture surface morphology of the cement stone at different locations after immersion in CO_2-saturated formation water at 80°C under high pressure: (a) 10 d, interfacial transition zone; (b) 10 d, matrix; (c) 30 d, interfacial transition zone; (d) 30 d, matrix; (e) 40 d, interfacial transition zone; (f) 40 d, matrix; (g) 60 d, interfacial transition zone; and (h) 60 d, matrix.

Figure 9 presents the fracture surface morphology of the cement stone after immersion for various times under the high pressure condition. The matrix of the cement stone is denser and more uniform at 10 days under the high pressure as compared to that under the normal pressure (Figure 9 (b)), indicating that high pressure promotes the hydration process of cement [14, 34]. At the immersion time of 30 days, the matrix of the cement stone is extremely dense (Figure 9 (d)), which is consistent with the highest mechanical strength obtained at 30 days. At the same time, a few $CaCO_3$ and pores are visible in the interfacial transition zone (Figure 9 (c)). It further validates high pressure not only promotes the hydration of cement, but also accelerates the diffusion rate of CO_2-related species through the cement. Barlet-Gouedard *et al.* reported that the degradation of concrete was rapid when exposed to CO_2-saturated formation water at high CO_2 pressures [45]. They determined that the concrete was not resistant enough to CO_2-saturated electrolyte because the dissolution process after the initial carbonation would lead to the formation of pores and further decrease the density of the concrete [45]. Under the high pressure condition, the CO_2-related species could reach the interfacial transition zone faster and predominantly accumulate at the interface of cement and casing steel [45]. According to the analysis of interfacial shear strength, the bonding strength between cement and casing steel is the highest at the time of 30 days (Figure 5), indicating that the amount of CO_2-related species accumulated in the interfacial transition zone is not enough to cause severe damage to the interface. After 40 days of immersion, micro-pores are visible in the matrix (Figure 9 (f)). In addition, more $CaCO_3$ and pores are observed in the interfacial transition zone (Figure 9 (e)), indicating the accumulation of CO_2-related species in the interfacial transition zone becomes pronounced, which may destabilize the interface of cement/casing. At the time of 60 days, the cement stone matrix becomes more porous, and more pores and $CaCO_3$ exist in the interfacial transition zone, indicating that a large amount of CO_2-related species has accumulated in the interfacial transition zone, and the carbonation of cement and corrosion of casing steel have basically destroyed the interface of cement/casing (Figure 9 (g)). It is obvious that the carbonation process in the interfacial transition zone is much severer under the high pressure as compared to that under the normal pressure [29]. Similar results were reported in the literatures [29, 32, 42, 43, 45].

3.3.2 Corrosion morphology of the casing steel after the test

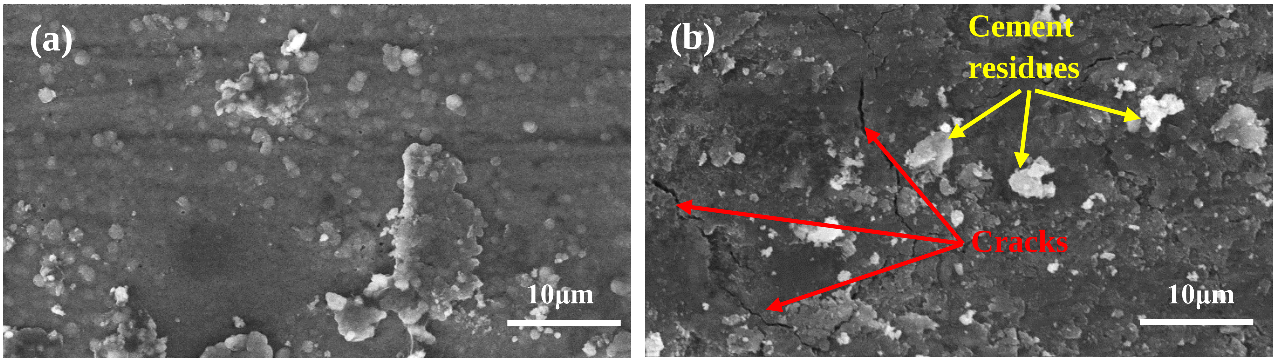

Figure 10. SEM observation of casing steel after immersion in CO_2-saturated formation water at 80°C for 60 days under (a) normal pressure, and (b) high pressure

Figure 10 shows the morphology of the casing steel removed from the cement stone after 60 days of immersion. The steel surface is composed of a layer of flat and compact corrosion products when tested under the normal pressure (Figure 10 (a)). Under the high pressure, the corrosion product layer is extremely rough accompanied with many cracks and some residual cement particles or $CaCO_3$ from the interfacial transition zone (Figure 10 (b)).

Generally, a layer of $FeCO_3$ scale could form on the surface when the steel is exposed to the CO_2-saturated oilfield formation water. The corrosion performance of the steel depends on the integrity and compactness of the scale, which is affected by temperature, pressure, and testing time [23]. When the scale is cracked, a galvanic effect exists between the steel surface (anode) and the scale-covered region (cathode) [47-49]. The big cathode vs. small anode geometry accelerates the local corrosion reaction, whereby corrosion pits formation is prone to occur [50-54]. Tavares et al. reported that a layer of $Fe_xCa_{1-x}CO_3$ with many defects would form with the presence of $CaCO_3$, which assisted the formation of pits on the steel surface [55]. In addition, the formation of a $Fe_xCa_{1-x}CO_3$ compound will compromise the protective properties of the corrosion scale because the replace of Fe by Ca induces a high stress in the lattice of $Fe_xCa_{1-x}CO_3$ [55, 56]. Therefore, the overwhelming accumulation of $CaCO_3$ in the interfacial transition zone under the high CO_2 partial pressure, could assist the formation of defected and rough corrosion product layer on the casing steel surface, leading to a high tendency of corrosion.

3.4 Corrosion products analysis of the casing steel

Energy spectrum, Raman spectra, and x-ray photoelectron spectroscopy were used to determine the composition of corrosion products on the surface of casing steel after 60 days of corrosion under the high pressure. According to EDS analysis, the corrosion products are composed of mainly Fe, C, O, Ca, and Si, as shown in Figure 11.

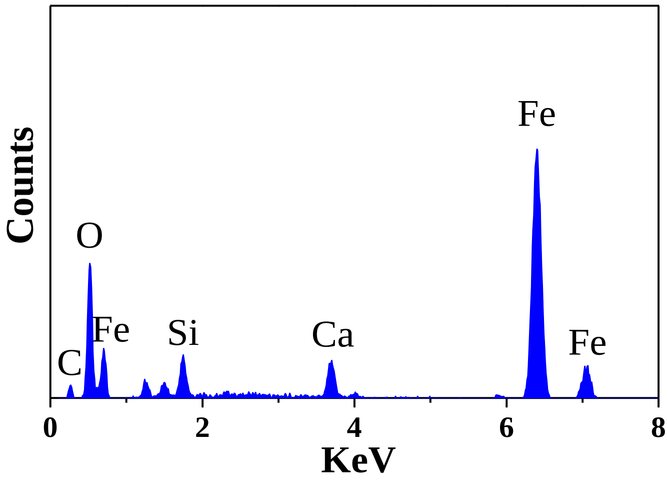

Figure 11. EDS results of corrosion products on the steel surface after immersion in CO_2-saturated formation water at 80°C under high pressure

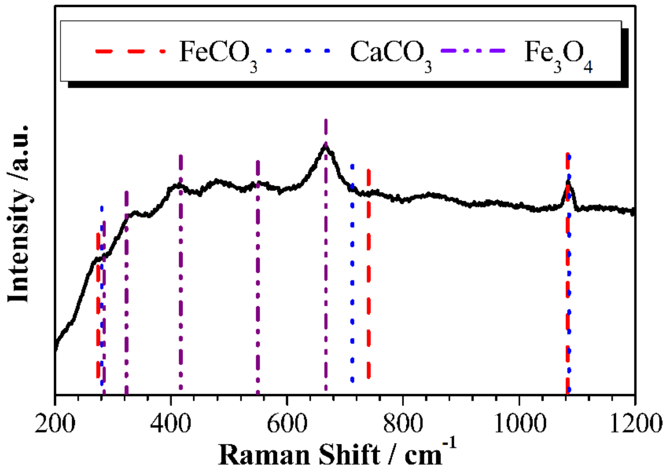

Figure 12. Raman spectrum of the corrosion products on the steel surface after immersion in CO_2-saturated formation water at 80°C under high pressure

Figure 12 shows Raman spectrum analysis of the corrosion products on the surface of the casing steel. Raman characteristic peaks of 667 cm^{-1} and 1084 cm^{-1} have been observed, which correspond to the characteristic peak of Fe_3O_4 and $FeCO_3$ (or $CaCO_3$), respectively [57-59]. As is reported, the peaks at about 276, 734, and 1084 cm^{-1} indicate the presence of $FeCO_3$, and the peaks at about 281, 712, and 1084 cm^{-1} indicate the presence of $CaCO_3$ [59, 60]. The peaks at about 288, 320, 420, 550, and 667 cm^{-1} indicate the presence of Fe_3O_4 [61]. It manifests that the corrosion products are predominantly $FeCO_3$, $CaCO_3$, and Fe_3O_4 when the casing steel is exposed to the CO_2-saturated oilfield formation water under the high pressure. The coexistence of $FeCO_3$ and $CaCO_3$ suggests the presence of a layer of $Fe_xCa_{1-x}CO_3$ (iron and calcium carbonate) scale on the steel surface under the high CO_2 pressure, which is consistent with previously results [55, 56].

Figure 13. shows x-ray photoelectron spectroscopy (XPS) analysis result of the corrosion product on the surface of casing steel. The full spectrum shows that the corrosion products are mainly composed of O, Fe, C, Cl, and Ca (Figure 13 (a)). The XPS spectrum of O is divided into three fitted peaks, as shown in Figure 13 (b). The binding energies are, respectively, 530.6 eV, 531.4 eV, and 531.6 eV, of which 530.6 eV corresponds to O^{2-}, 531.4 eV corresponds to O in CO_3^{2-}, and 531.6 eV corresponds to O in OH^-. The XPS spectrum of Fe can also be divided into three fitted peaks, where 709.2 eV corresponds to Fe^{2+}, 710.2 eV corresponds to Fe in $FeCl_2$, and 711.0 eV corresponds to Fe^{3+} [62, 63].

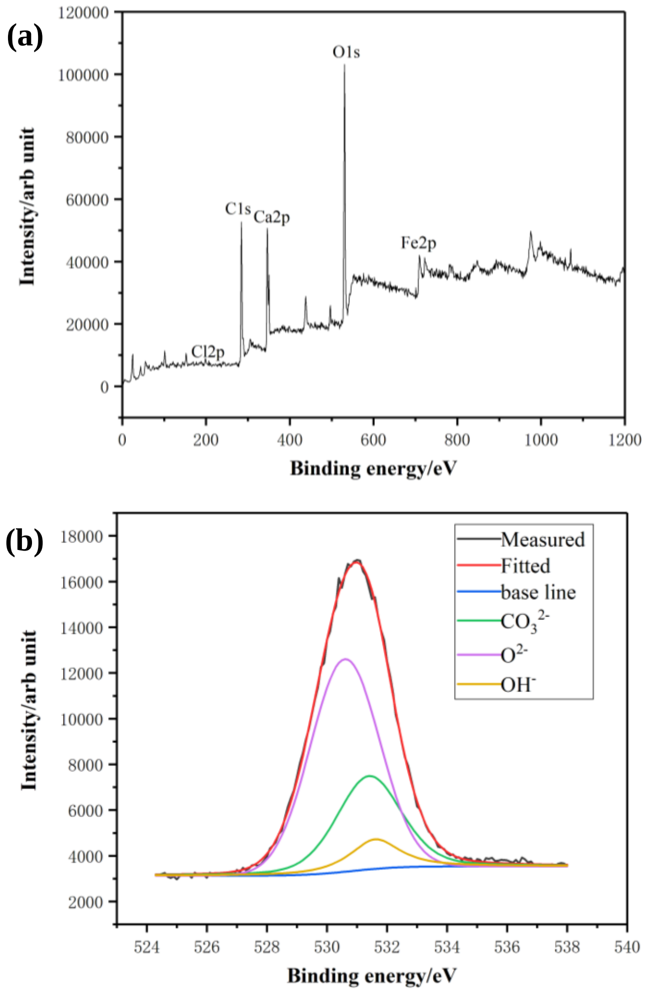

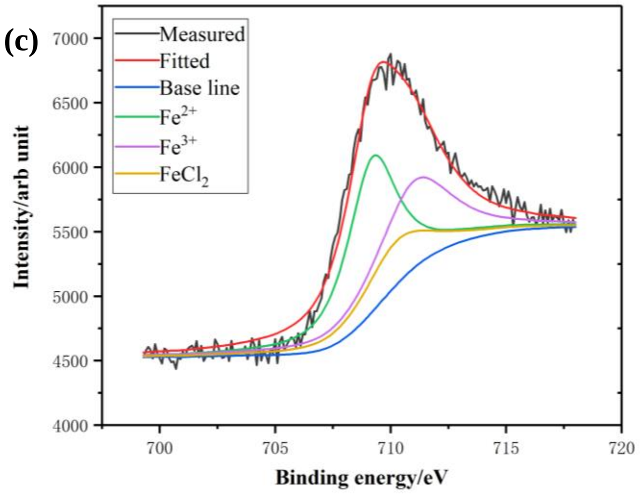

Figure 13. XPS spectrum and peak fitting of the corrosion products at casing steel surface after immersion in CO_2-saturated formation water at 80°C under high pressure: (a) full spectrum; (b) O spectrum; and (c) Fe spectrum

From the above analysis, the surface corrosion products of casing steel are mainly composed of $FeCO_3$ (with $Fe_xCa_{1-x}CO_3$), Fe_3O_4, and a small amount of $Fe(OH)_2$. Note that the detected $FeCl_2$ is an intermediate product generated during the catalytic corrosion of steel by Cl^-. The corrosion mechanism of steel by Cl^- is elaborated below to rationalize the presence of Fe_3O_4, $Fe(OH)_2$, and $FeCl_2$ in the corrosion products [64, 65].

$$Fe \rightarrow Fe^{2+}+2e \qquad (5)$$

$$2Cl^-+Fe^{2+} \rightarrow FeCl_2 \qquad (6)$$

$$FeCl_2+2H_2O \rightarrow Fe(OH)_2+2Cl^-+2H^+ \qquad (7)$$

$$6FeCl_2+O_2+6H_2O \rightarrow 2Fe_3O_4+12Cl^-+12H^+ \qquad (8)$$

It is worth noting that the testing solution was purged with CO_2, where O_2 was removed completely. However, the O_2-related corrosion process can exist in the following scenarios: 1) during the cement/casing sample preparation process when Cl^- and O_2 were available in the cement; 2) after corrosion but before mechanical testing, corrosion continues as long as the cement was wet and exposed to the air; and 3) after all the tests, the casing steel surface could inevitably suffer further corrosion due to the concurrent effect of water vapor and O_2 in the atmospheric air. Therefore, a small number of iron oxides, such as Fe_3O_4, could be detected in the corrosion products.

SEM observation has suggested that a layer of $FeCO_3$ (with $Fe_xCa_{1-x}CO_3$) scale forms on the steel surface after exposure to the CO_2-saturated oilfield formation water. In this work, the corrosion behavior of casing steel in the cement/casing system is predominantly affected by the CO_2, besides the Cl^- as discussed above. The corrosion mechanism related to CO_2 is shown in Figure 14 [36].

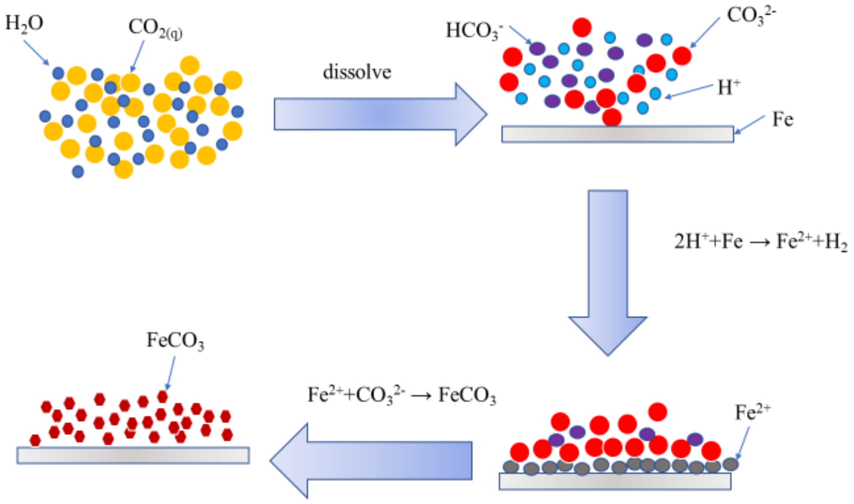

Figure 14. Illustration of steel corrosion in an aqueous solution saturated with CO_2

When the simulated formation water was purged with CO_2 gas, carbonic acid (H_2CO_3) will be generated through the following reaction:

$CO_2 + H_2O \leftrightarrow H_2CO_3$ (9)

The H_2CO_3 will be dissociated into HCO_3^- and carbonate CO_3^{2-} by the processes:

$H_2CO_3 \leftrightarrow H^+ + HCO_3^-$ (10)

$HCO_3^- \leftrightarrow H^+ + CO_3^{2-}$ (11)

The Fe^{2+} is prone to be generated through Reaction (5). With increasing the concentration of Fe^{2+} and CO_3^{2-}, the precipitation of $FeCO_3$ can readily occur by Reaction (12):

$Fe^{2+} + CO_3^{2-} \rightarrow FeCO_3$ (12)

The iron and calcium carbonate ($Fe_xCa_{1-x}CO_3$) could be formed through the following reactions:

$Fe^{2+} + Ca^{2+} + CO_3^{2-} \rightarrow Fe_xCa_{1-x}CO_3$ (13)

$Fe^{2+} + Ca^{2+} + HCO_3^- \rightarrow Fe_xCa_{1-x}CO_3 + H^+$ (14)

The Ca^{2+} was either from the diffusion from solution to the cement/casing interface, or from the product of carbonation process of the cement (Reaction (3)). Note that a high concentration of HCO_3^- will accelerate the formation of $Fe_xCa_{1-x}CO_3$ (Reaction (14)).

Based on EIS analysis, the R_c and R_{ct} values are quite small after 60 days of immersion, thereby promoting the diffusion of CO_2-related species through the cement and dissolution of the steel. The accumulated CO_2-related species at the interface of cement/casing accelerate the corrosion rate of the steel and lead to the precipitation of $FeCO_3$ when the concentration of Fe^{2+} and CO_3^{2-} is high enough. The structure and property of the $FeCO_3$ affect the further corrosion of the steel. A high pressure (or partial pressure) of CO_2 means a higher solubility of CO_2 in solution, whereby the diffusion-driven force of CO_2 is larger, resulting in a higher concentration of CO_2-related species (CO_3^{2-} and HCO_3^-) at the cement/casing interface. The higher concentration of HCO_3^- would induce the formation of $Fe_xCa_{1-x}CO_3$ (through Reaction (14)) and acidify the interface. The severe corrosion and appreciable precipitation of $CaCO_3$ in the interfacial transition zone would increase the stress and hence impact the integrity of the formed $FeCO_3$ (with $Fe_xCa_{1-x}CO_3$) layer on the steel surface (Figure 9). In addition, the vast accumulation of $CaCO_3$ in the interfacial transition zone could further assist the formation of $Fe_xCa_{1-x}CO_3$ products with defects on the casing steel surface [55]. Under these circumstances, the corrosion product layer on the steel surface is much rougher and composed of more defects under the high CO_2 pressure, whereby the corrosion severity of the steel is greatly enhanced (Figure 10).

It has been reported that the $FeCO_3$ or $Fe_xCa_{1-x}CO_3$ products are prone to precipitate at flawed locations of corrosion product scale where Fe^{2+} ions will be accumulated gradually [47]. The precipitation could create a capped enclosure that blocks the path of mass transport to and from the surrounding solution, thereby promoting the formation of pits [47]. The anodic dissolution of steel continues because the flow of electrons from the steel surface to the cathodic regions is possible in the presence of a flawed corrosion product layer. The increase in the concentration of Fe^{2+} ions and the subsequent hydrolysis of Fe^{2+} ions, could increase the concentration of H^+ ions in the localized area where Cl^- ions are prone to accumulate to maintain the charge balance (Eq. 15).

$$Fe^{2+}+2H_2O \rightarrow Fe(OH)_2+2H^+ \qquad (15)$$

The above processes would increase the acidity of the localized areas where the dissolution of steel and a fast formation of pits would be significantly enhanced [66, 67]. Under the high pressure of CO_2, the cement matrix will be porous due to the carbonation process, facilitating the diffusion of Cl^- to the interface of cement/casing [68]. The accumulation of Cl^- at the interface further deteriorates the corrosion performance of the casing steel (such as increasing the pitting tendency). Therefore, the casing steel was severely corroded after immersion under the high pressure of CO_2.

4. CONCLUSIONS

The corrosion behavior and mechanical properties of a concrete/P110 casing steel system were studied in a simulated, CO_2-saturated formation water under different CO_2 partial pressures. Main findings from the investigation have been drawn below:

(1) The corrosion behavior of cement is influenced by both the hydration and carbonation processes, which makes the corrosion resistance of cement increase initially and then decline gradually. The corrosion resistance of the casing steel invariably decreases with immersion time. With an increase in the CO_2 pressure, the reduction in corrosion resistance of cement and the casing steel is much more noticeable.

(2) The interfacial transition zone and the matrix of cement show the same trend in the decrease of the mechanical properties, including interfacial shear strength, micro-hardness, and compressive strength. The properties of interfacial transition zone and matrix of cement begin to decrease when the carbonation process is dominant.

(3) The structure of cement becomes dense due to the hydration of cement, whereas the carbonation process will introduce pores and defects in the cement. $CaCO_3$ precipitation and pore-formation in the interfacial transition zone reduce the cementation strength at the cement/casing interface.

(4) The composition of the corrosion products on the casing steel surface is mainly $Fe_xCa_{1-x}CO_3$, Fe_3O_4, and a small amount of $Fe(OH)_2$.

(5) With an increase in the CO_2 partial pressure, the degradation of cement and cement/casing interface was aggravated, which assisted the formation of a defected corrosion product layer and led to severer corrosion on the casing steel surface.

ACKNOWLEDGEMENTS

This work was supported by Guangxi Key Laboratory of Information Materials (Guilin University of Electronic Technology), P.R. China (Project No. 191009-K), and Scientific Research Foundation and Opening Foundation (X151519KCL09) of Southwest Petroleum University.

References

1. H. Ji, Y. Tian, R. Zhao, N. Jin, X. Jin, Z. Tian, D. Yan and H. Ye, *Int. J. Electrochem. Sci.*, 15 (2020) 6488.
2. Y. Peng, L. Liu, S. Wang, Y. Lin, Y. Sun and R. Xia, *J. Petrol. Sci. Eng*., 167 (2018) 949.
3. D. Hou, X. Xu, M. Wang, Z. Chen, J. Zhang, B. Dong, J. Miao and C. Liu, *Appl. Surf. Sci.*, 514 (2020) 145898.
4. S. Pang, B. Diao and Y. Ye, *Int. J. Electrochem. Sci*., 12 (2017) 5539.
5. C. Bai, S. Liu, F. Ma, S. Lu, J. Wang and S. Liu, *Int. J. Electrochem. Sci*., 15 (2020) 4660.
6. J. Wang, S. Qian, Y. Li, D.D. Macdonald, Y. Jiang and J. Li, *J. Mater. Sci. Technol*., 35 (2019) 637.
7. B. Simmons, World oil, 229 (2008).
8. X. Zhou, X. Lin, M. Huo and Y. Zhang, *Cement Concrete Res.*, 26 (1996) 1753.
9. X. Zhang, B. Wu, J. Zhang, J. Li, S. Wang, L. Dong, L. Liu and D. Xiang, *Int. J. Electrochem. Sci*., 14 (2019) 10693.
10. X. Feng, Y. Xu, X. Zhang, X. Lu, R. Shi, L. Zhang, J. Zhang and D. Chen, *Int. J. Electrochem. Sci*., 14 (2019) 3494.
11. S. Horpibulsuk, W. Phojan, A. Suddeepong, A. Chinkulkijniwat and M.D. Liu, *Appl. Clay. Sci*., 55 (2012) 44.
12. C. Teodoriu and P. Asamba, *J. Nat. Gas Sci. Eng*., 24 (2015) 324.
13. M. Wigand, J.P. Kaszuba, J.W. Carey and W.K. Hollis, *Chem. Geol.*, 265 (2009) 122.
14. B.G. Kutchko, B.R. Strazisar, D.A. Dzombak, G.V. Lowry and N. Thaulow, *Environ. Sci. Technol*., 41 (2007) 4787.
15. R. Rizzo, S. Gupta, M. Rogowska and R. Ambat, *Corros. Sci.*, 162 (2020) 108214.
16. B. Xu, B. Yuan, Y. Wang and L. Zhu, *Constr. Build. Mater*., 188 (2018) 161.
17. T. Gu, X. Guo, Z. Li, X. Cheng, X. Fan, A. Korayem and W.H. Duan, *Constr. Build. Mater*., 130 (2017) 92.
18. S. Wang, F. Wang, F. Xu, M. Bao, L. Liu, X. Wang and C. Ren, *Int. J. Electrochem. Sci*., 12 (2017) 10084.
19. D.M. Ortega-Toledo, J.G. Gonzalez-Rodriguez, M. Casales, L. Martinez and A. Martinez-Villafañe, *Corros. Sci.*, 53 (2011) 3780.
20. S. Wang, L. Wang, X. Liu, M. Bao, L. Liu, X. Wang and C. Ren, *Int. J. Electrochem. Sci*., 12 (2017) 10317.
21. F. Wang, S. Lei, J. Ou and W. Li, *Appl. Surf. Sci*., 507 (2020) 145016.
22. F. Dalla Vecchia, V.H.J.M. dos Santos, M.K. Schütz, G.G.D. Ponzi, A.S.d.G.e. Stepanha, C.d.F. Malfatti and E.M.d. Costa, *Intl. J. Greenh. Gas Con*., 98 (2020) 103077.
23. G.A. Zhang and Y.F. Cheng, *Electrochim. Acta*, 56 (2011) 1676.
24. R. Barker, I. Al Shaaili, R.A. De Motte, D. Burkle, T. Charpentier, S.M. Vargas and A. Neville, *Appl. Surf. Sci*., 469 (2019) 135.
25. Y. Hua, S. Mohammed, R. Barker and A. Neville, *J. Mater. Sci. Technol.*, 41 (2020) 21.

26. Z. Tan, L. Yang, D. Zhang, Z. Wang, F. Cheng, M. Zhang and Y. Jin, *J. Mater. Sci. Technol*., 49 (2020) 186.
27. Y. Jiang, X.-l. Gong, J. Dai, H.-m. Meng and B. Long, *Int. J. Electrochem. Sci*., 15 (2020) 2973.
28. R. Barker, D. Burkle, T. Charpentier, H. Thompson and A. Neville, *Corros. Sci.*, 142 (2018) 312.
29. Y.-S. Choi, D. Young, S. Nešić and L.G.S. Gray, *Intl. J. Greenh. Gas Con*., 16 (2013) S70.
30. J. Shi, W. Sun and J. Ming, *Procedia Eng*., 27 (2012) 412.
31. X. Wang, W. Jihui and X. Yue, *Int. J. Electrochem. Sci*., 9 (2014) 6558.
32. M.F. Montemor, M.P. Cunha, M.G. Ferreira and A.M. Simoes, *Cement Concrete Comp*., 24 (2002) 45.
33. M. Nobial, O. Devos, O.R. Mattos and B. Tribollet, *J. Electroanal. Chem*., 600 (2007) 87.
34. S. Ma and S. Kawashima, *Constr. Build. Mater*., 215 (2019) 119.
35. H.B. Gunay, O.B. Isgor and P. Ghods, *Corrosion*, 71 (2015) 615.
36. J. Han, J. Zhang and J.W. Carey, *Intl. J. Greenh. Gas Con*., 5 (2011) 1680.
37. N.J. Welch, L.P. Frash, D.H. Harp and J.W. Carey, *Intl. J. Greenh. Gas Con*., 95 (2020) 102977.
38. J.W. Carey, M. Wigand, S.J. Chipera, G. WoldeGabriel, R. Pawar, P.C. Lichtner, S.C. Wehner, M.A. Raines and G.D. Guthrie Jr, *Intl. J. Greenh. Gas Con*., 1 (2007) 75.
39. D. Velissariou, N. Katsiotis, P. Tsakiridis, M. Katsiotis, N. Pistofidis, K. Kolovos and M. Beazi, *Constr. Build. Mater.*, 197 (2019) 63.
40. G. Fajardo, P. Valdez and J. Pacheco, *Constr. Build. Mater*., 23 (2009) 768.
41. S.-C. Kou, B.-j. Zhan and C.-S. Poon, *Cement Concrete Comp*., 45 (2014) 22.
42. S.O. Ekolu, *Constr. Build. Mater*., 127 (2016) 306.
43. D.C. Park, *Constr. Build. Mater*., 22 (2008) 2260.
44. H. Abdoulghafour, L. Luquot and P. Gouze, *Environ. Sci. Technol*., 47 (2013) 10332.
45. V. Barlet-Gouedard, G. Rimmele, B. Goffe and O. Porcherie, Mitigation strategies for the risk of CO_2 migration through wellbores, in, Society of Petroleum Engineers.
46. H. Satoh, S. Shimoda, K. Yamaguchi, H. Kato, Y. Yamashita, K. Miyashiro and S. Saito, *Energy Procedia*, 37 (2013) 5781.
47. S. Wang, L. Lamborn, K. Chevil, E. Gamboa and W. Chen, *J. Mater. Sci. Technol.*, 49 (2020) 166.
48. L. Shi, X. Yang, Y. Song, D. Liu, K. Dong, D. Shan and E.-H. Han, *J. Mater. Sci. Technol*., 35 (2019) 1886.
49. A.I. Ikeuba, B. Zhang, J. Wang, E.-H. Han and W. Ke, *J. Mater. Sci. Technol*., 35 (2019) 1444.
50. S. Wang, L. Lamborn, K. Chevil, E. Gamboa and W. Chen, *Corros. Sci.*, (2020) 108592.
51. M. Wang, C. Qiao, X. Jiang, L. Hao and X. Liu, *J. Mater. Sci. Technol*., 51 (2020) 40.
52. S.D. Wang, D.K. Xu, B.J. Wang, L.Y. Sheng, Y.X. Qiao, E.-H. Han and C. Dong, *Corros. Sci*., 142 (2018) 185.
53. S. Wang, D. Xu, B. Wang, E. Han and C. Dong, *Mater. Design*, 84 (2015) 185.
54. B.J. Wang, D.K. Xu, S.D. Wang, L.Y. Sheng, R.-C. Zeng and E.-h. Han, *Int. J. Fatigue*, 120 (2019) 46.
55. L.M. Tavares, E.M.d. Costa, J.J.d.O. Andrade, R. Hubler and B. Huet, *Appl. Surf. Sci*., 359 (2015) 143.
56. Z.D. Cui, S.L. Wu, S.L. Zhu and X.J. Yang, *Appl. Surf. Sci.*, 252 (2006) 2368.
57. L. Wei, X. Pang and K. Gao, *Corros. Sci*., 103 (2016) 132.
58. A. Sumoondur, S. Shaw, I. Ahmed and L.G. Benning, *Mineral. Mag*., 72 (2008) 201.
59. K. Sanjiv Raj, N. Devi and V.K. Subramanian, *Chem. Phys. Lett*., 750 (2020) 137502.
60. C.T. Lee, M.S. Odziemkowski and D.W. Shoesmith, *J. Electrochem. Soc*., 153 (2006) B33.
61. D. Neff, S. Reguer, L. Bellot-Gurlet, P. Dillmann and R. Bertholon, *J. Raman. Spectrosc*., 35 (2004) 739.
62. C. Li, Y. Xiang, C. Song and Z. Ji, *J. Supercrit. Fluids*, 146 (2019) 107.
63. L. Wei, K. Gao and Q. Li, *Appl. Surf. Sci*., 440 (2018) 524.
64. K. Thangavel and N.S. Rengaswamy, *Cement Concrete Comp*., 20 (1998) 283.

65. J. Wei, X.X. Fu, J.H. Dong and W. Ke, *J. Mater. Sci. Technol.*, 28 (2012) 905.
66. B. Zhang and X.L. Ma, *J. Mater. Sci. Technol.*, 35 (2019) 1455.
67. F. Xue, X. Wei, J. Dong, C. Wang and W. Ke, *J. Mater. Sci. Technol.*, 35 (2019) 596.
68. Y. Wang, H. Zhou and Y. Zhang, *Int. J. Electrochem. Sci.*, 15 (2020) 3232